



# Wide-field OCT angiography for non-human primate retinal imaging

XIANG WEI,<sup>1,2</sup> TRISTAN T. HORMEL,<sup>2</sup> LAURIE RENNER,<sup>3</sup> MARTHA NEURINGER,<sup>2,3,4</sup> AND YALI JIA<sup>1,2,5</sup>

<sup>1</sup>Department of Biomedical Engineering, Oregon Health & Science University, Portland, OR, 97239, USA

<sup>2</sup>Casey Eye Institute, Oregon Health & Science University, Portland, OR, 97239, USA

<sup>3</sup>Oregon National Primate Research Center, Oregon Health & Science University, Beaverton, OR, 97006, USA

<sup>4</sup>[neuringe@ohsu.edu](mailto:neuringe@ohsu.edu)

<sup>5</sup>[jiaya@ohsu.edu](mailto:jiaya@ohsu.edu)

**Abstract:** Optical coherence tomography (OCT) is a well-established research tool for vision research in animal models capable of providing *in vivo* imaging of the retina. Structural OCT can be enhanced using OCT angiography (OCTA) processing in order to provide simultaneously acquired, automatically co-registered vascular information. Currently available OCT. Currently available OCTA lack either large field of view or high resolution. In this study we developed a wide-field (60-degree), high-resolution (10.5-μm optical transverse) and high-sensitivity (104-dB) OCTA-enabled system for non-human primate imaging and with it imaged multiple disease models, including models of age-related macular degeneration (AMD), Bardet-Biedl Syndrome (BBS), and the *CLN7* variant of Batten disease. We demonstrate clear visualization of features including drusen, ellipsoid zone loss, vascular retinopathy, and retinal thinning in these eyes.

© 2024 Optica Publishing Group under the terms of the [Optica Open Access Publishing Agreement](#)

## 1. Introduction

Optical coherence tomography (OCT) is an interferometric imaging modality based on analyzing an optical signal backscattered by tissue [1]. It provides high-resolution imaging approaching the micron-scale in both axial and transverse directions. Combined with millimeter-scale imaging depths this makes OCT an ideal technology for visualizing the retina. These capabilities have made OCT technology essential for retinal disease diagnosis in the clinic [2], and can be contrasted with other vascular imaging modalities such as color fundus photography or dye-injection that do not acquire images that are as readily interpretable. Furthermore, modern systems are also capable of achieving OCT angiography (OCTA) by measuring the difference between two rapidly acquired cross-sectional scans. This capability allows the structural anatomic information accrued by (reflectance) OCT to be paired with vascular information provided by OCTA collected in a single procedure.

For these reasons, OCT has found wide application in the ophthalmic and vision research communities [3,4]. Among the research uses of OCT technology is imaging in animal models, which provide uniquely controlled environments for interrogating disease pathophysiology and etiology. Animal models including mice [5], rats [6], and rabbits [7] have been investigated with OCT. However, a major limitation of these models for making analogies with human retinal disease pathologies and visual function is the lack of a macula. The macula is responsible for humans' central, high-acuity vision and is of paramount importance in vision loss associated with two of the most prevalent blinding diseases, age-related macular degeneration (AMD) and diabetic macular edema [8,9]. Relative to other animal models, non-human primates (NHPs) offer the closest anatomic analogy to humans, since among research organisms they are unique in possessing maculas. They also provide well-established models of many human disorders, having been used in studies of several diseases [10]. In particular, we have previously explored

naturally-occurring NHP models of AMD from the early stage to the late stage [11], Bardet-Biedl Syndrome (BBS) [12], and a *CLN7* variant of Batten disease [13].

While OCT imaging of these models has proven useful, some key limitations remain to be overcome. Chief among these is a fundamental, unavoidable scanning-speed-limited trade-off between system resolution and field-of-view, by which we mean both the transverse and axial imaging dimensions. Both of these design parameters are important: field-of-view for identifying far-flung pathologic features located at widely separated regions of the retina or from the vitreous to the choroid, and high-resolution for detecting small pathologic features, which are often the first anatomic manifestations of disease or precursors of treatment indicators. Due to their role in exploratory studies, it is arguably especially important that NHP equivalents of pre-clinical pathologic features can be assessed if such models are to be optimally used to enhance our understanding of disease etiology. For these reasons, we sought to develop a high-speed device that could avoid sacrificing either a large field of view or high resolution. Starting with the transition from time domain to Fourier domain systems [14,15], many substantial improvements in OCT technology have resulted from improvements to system scan acquisition speeds. Today, the fastest devices are swept source OCT [16,17]. Systems that achieve up to a hundred-degree field-of-view have been proposed, but lack OCTA capabilities [18]. Furthermore, contemporary alternatives that incorporate OCTA usually rely on multiple fixation targets, as in for example Neiderleithner et al. [19]. But imaging schemes that rely on multiple fixation targets are arduous for imaging anesthetized model organisms. The priorities for NHP imaging are different. While high system acquisition speeds are essential for human imaging in which the imaging subject is not typically anesthetized, for NHP imaging we can sacrifice some imaging speed due to the much smaller intensity of motion artifacts that are already minimized through anesthesia. Still, it should be noted that the linear regime in flow signal constrains interscan times [20]. Therefore system speed is still a useful parameter in NHP imaging, and along with rapid scan acquisition, other advantages of swept source OCT systems include an extended imaging depth [21,22] and long coherence length plus a high overall signal-to-noise ratio thanks to the application of a balanced detection technique [23]. These advantages do not come free of complications. In a swept source OCT system, the signal is recorded sequentially, and for each individual A-line, a trigger signal is needed to initiate data acquisition, which introduces phase errors that must be corrected with hardware or in software [24–27]. In addition to phase stabilization, the system should achieve high sensitivity to compensate for signal attenuation in deeper tissues especially for peripheral imaging where attenuation can be more severe, and reduce the number of sampling positions needed to achieve high-resolution images. Artifacts should also be compensated. In particular, in OCTA revealing details from individual plexuses requires projection artifact removal [28].

In the study, we built a wide-field swept source OCTA platform designed for NHP retinal imaging that addresses these concerns, and used it to explore NHP models of AMD, BBS, and Batten disease.

## 2. Methods

### 2.1. 200-kHz swept source OCT system

In this study, we constructed a 200-kHz swept source OCT system (Fig. 1(A)). The opto-mechanical elements were designed using computer-aided design (CAD) software (Solidworks), and fused deposition modeling (FDM) 3D printing was used to fabricate the mechanical parts on site. Polylactic acid (PLA) was used as the 3D printing material due to its ease of handling. The system was printed at a maximum of 50- $\mu\text{m}$  layer resolution, as needed (UltiMaker S5). The imaging system was packaged on a roller table, with the laser and computer positioned underneath. The box containing the opto-mechanical elements was installed on a slit lamp mount with a chin rest (Fig. 1(D)).

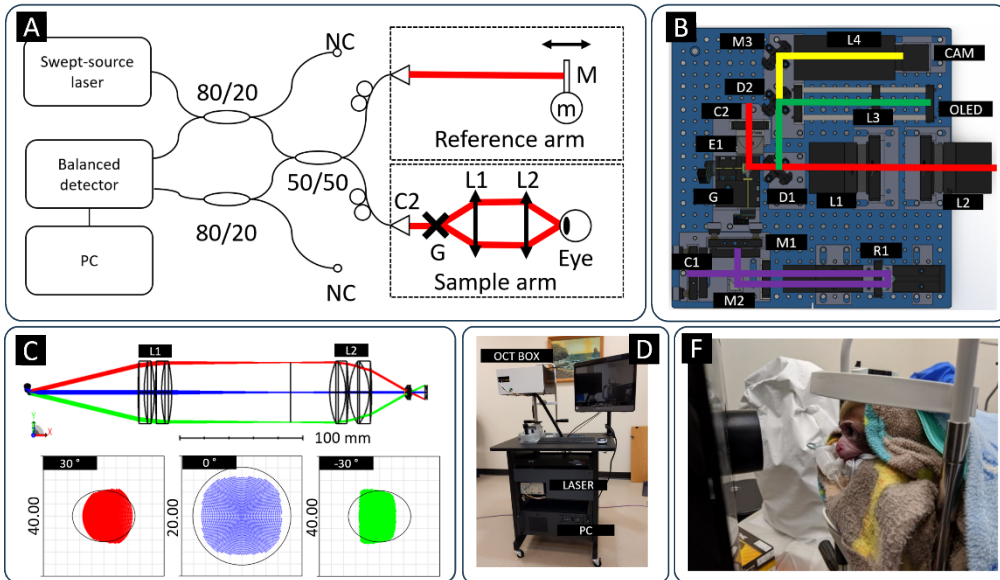


**Fig. 1.** 200-kHz wide-field swept source OCT system. (A) Diagram of the system design. The wavelength-tuning laser light is first coupled into the OCT system using an 80/20 fiber optic coupler. Twenty percent of the power is split into the reference arm and the sample arm. In the reference arm, a customized motorized optical delay line is used to change the length of the optical path. A set of customized lenses is used in the reference arm to acquire 60-degree field-of-view images. The reflected light from both the reference arm and the sample arm interferes in the 50/50 coupler. The interference signal is then collected by a balanced photodetector, and the signal is acquired by a digitizer and processed by a PC. (B) 3D modeling of the OCT system: The red line indicates the optical path of the sample arm, the green line indicates the optical path of the fixation target, the yellow line indicates the optical path of the pupil camera, and the purple line indicates the optical path of the reference arm. Because animals were anesthetized, the fixation target was used only for system development. C1 is the reference arm collimator, M1, M2, and M3 are protected silver-coated mirrors, C2 is the sample arm collimator, E1 is an electrically tunable lens, G is a galvanometer scanner, D1 and D2 are dichroic mirrors. (C) Optical simulation (OpticStudio, Zemax) of the sample arm telescope: L1 and L2 are two customized lens sets. The lenses were designed based on simulation with this software. The red line indicates the +30° scanning light, blue indicates the 0° scanning light, and green indicates the -30° scanning light. The corresponding spot diagrams indicate that this system can achieve diffraction-limited imaging throughout the imaging field. (D) The complete system setup from the operator's perspective: both OCT reference and sample arms are in the OCT box. The laser and a PC are embedded under the table. (F) A non-human primate being imaged with the device.

The key device employed in this system is a vertical cavity surface emitting laser (VCSEL) with an external micro-electromechanical system (MEMS)-based tunable cavity. This type of laser is well-suited for OCT imaging due to its high output power and broad tuning range. The center wavelength of the laser was 1060 nm with a 100 nm bandwidth. The maximum axial resolution was 5  $\mu\text{m}$  in the air, which allows for high-resolution imaging of tissue microstructure. The laser engine had an integrated sampling clock that allowed it to acquire 1536 samples per A-scan, corresponding to a 4 mm imaging depth in air. The input laser light was attenuated using a 20/80 fiber optic coupler, which ensured that the light intensity was suitable for retinal imaging.

The power induced was measured as 2 mW, which meets American National Standards Institute safety recommendations (ANSI Z136.1-2000) [29].

Similar to our previously developed instrument for human imaging [30,31], the system design was based on Michelson interferometry which is a well-established and widely used configuration in OCT imaging. The Michelson interferometer included both a reference arm and a sample arm to generate an interference pattern, which was processed to construct the OCT volume; the sample arm collected light reflected from the NHP eye. Illumination was split evenly between the reference and sample arms by a 50/50 fiber optic coupler. To achieve high reliability and a small form of factor, the reference arm and sample arm were integrated into a single 12" × 12" breadboard (Fig. 1(B)) with a maximum height of 6".

The reference arm contained a stepper motor linear actuator (NEMA 14) that used a customized controller to enable fast and accurate tuning of the reference arm length. The communication between the controller and the PC was handled by an ARM cortex M3 microcontroller (STM32, STMicroelectronics), and the stepper motor was directly driven by a micro-stepping motor driver chip (A4988, Allegro). Combined with the 1-mm lead screw pitch and 200 steps per revolution, a maximum of 5- $\mu\text{m}$  step resolution was achieved. A retroreflector was positioned on the linear actuator to control the optical path length without introducing alignment errors.

The sample arm was positioned in the middle of the breadboard. A 4 mm collimator induced collimated light to the galvanometer scanner. A pair of 5 mm scanner mirrors were used for both the X- and Y-directions. Diffraction-limited resolution was achieved at both the center imaging field and 30° imaging angle by utilizing a customized lens set in the sample arm telescope, and a total imaging field of 60° could be acquired in a single shot (Fig. 1(C)). The effective focal lengths of the scanning lens and imaging lens were 100-mm and 50-mm, respectively. This lens set was optimized for the NHP eye based on a human eye model provided by the optical design software, OpticStudio (Zemax), used for simulations, modified to include an axial length of 18 mm, equivalent to 75% of the size of a human eye (Table 1). The theoretical optical transverse resolution of this device is 10.5- $\mu\text{m}$ .

**Table 1. Detailed parameters of NHP eye model. The “NA” values in the retina simulation indicate that this parameter was not used (because light propagating through the retina was not simulated)**

Anatomic Region	Radius (mm)	Thickness (mm)	Conic Parameter	Refractive Index
Cornea	7.8	0.52	-0.5	1.32
Aqueous	6.7	2.13	-0.3	1.40
Lens	7.0	3.23	0	1.36
Vitreous	-5.3	12.29	-3.5	1.32
Retina	-11.0	NA	NA	NA

The reflected light from both the reference arm and sample arm was collected by a balanced photodiode, which ensured high sensitivity and accurate detection of the reflectance signal. A high-speed digitizer (ATS9360) was used to convert the electrical signal into a digital signal at 0.3 GS/s. The acquired OCT signal was then processed using an Nvidia GTX1080ti graphics card that could handle large amounts of data in real time.

Although not used for data acquisition in this report (NHPs were anesthetized during imaging), our system also included a fixation target and pupil camera that was employed during development to help with instrument alignment. These elements were optically coupled to the OCT main optical path by a dichroic mirror positioned in between the scanning lens and the galvanometer scanner. An infrared filter on the pupil camera (AmScope, MD310-BS) could be removed to enhance the sensitivity in the near infrared range. A pair of LEDs with 910 nm wavelength

illuminated the pupil. The OLED fixation target was also controlled by the same microcontroller that controlled the reference arm stepper motor.

### 2.2. Non-human primate models

Rhesus macaques (*Macaca mulatta*) and a Japanese macaque (*Macaca fuscata*) from the Oregon National Primate Research Center (ONPRC) colony were included in this study.

### 2.3. Animal preparation

Prior to imaging, animals were anesthetized by an intramuscular injection of Telazol (1:1 mixture of tiletamine hydrochloride and zolazepam hydrochloride, 3.5–5.0 mg/kg) followed by intubation and administration of inhalant isoflurane (1 – 2%) vaporized in 100% oxygen. Pupils were fully dilated with 1% tropicamide and 2.5% phenylephrine eyedrops, and eyes were fitted with speculums and plano contact lenses.

### 2.4. Image processing

OCT images were acquired and processed during imaging sessions using our previously developed real-time OCT/OCTA imaging processing software [32]. The raw spectrum was first acquired by the digitizer (ATS9360, Alazar Technologies) and transferred to the computer host memory batch by batch. Each batch contained 16 B-scans. After the host computer received each batch, it was then transferred to the GPU's device memory for signal processing. For each OCT B-scan, the data was first processed by subtracting the mean of each A-scan to suppress low frequency noise. Then a digital algorithm was applied to compensate for dispersion mismatch between the reference arm and the sample arm. The raw spectrum was then further processed using standard OCT image reconstruction algorithms to generate the volumetric images [33]. At the same time, the raw OCT spectral data was also processed using our previously developed phase-stabilized complex-decorrelation angiography algorithm [26] to generate a high-resolution phase-stabilized OCTA image. This method compensates for phase instability during data acquisition. To generate OCTA data we used three repeat scans. Both OCT and OCTA cross-sectional and *en face* images were displayed in a user interface to guide the operator during data acquisition. The OCT and OCTA volumes were then segmented into different layers (nerve fiber layer, superficial vascular complex, deep capillary plexus, choroidal layer; Fig. 2) using our previous developed COOL-ART software [34,35]. *En face* OCT/OCTA images projected from different retinal slabs could then be generated [36].

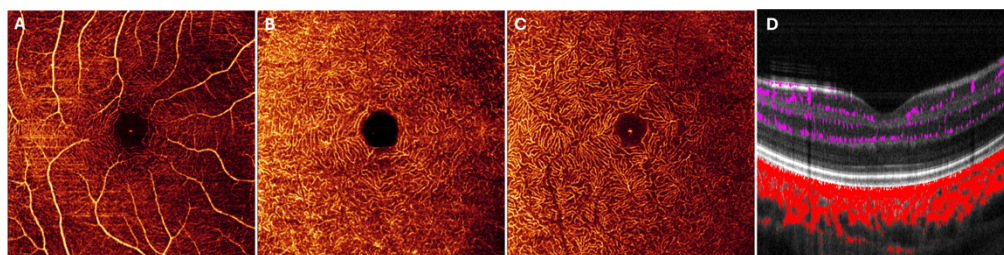


**Fig. 2.** Images from a healthy non-human primate. (A) superficial vascular complex; (B) intermediate capillary plexus; (C) deep capillary plexus; (D) cross section with flow signal overlaid (violet: retinal; red: choroidal).

### 3. Results

#### 3.1. Healthy individual

We begin with example images from a healthy individual to contrast with the other cases shown below.

#### 3.2. Bardet-Biedl syndrome

Bardet-Biedl syndrome (BBS) is an inherited ciliopathic disorder that can result in progressive retinal degeneration, obesity, polydactyly, renal anomalies, genital abnormalities and intellectual disabilities [37–39], as well as other variable symptoms that develop, with the exception of polydactyly, in the first or second decade of life. In the eye, BBS is thought to cause dysfunction in the cilium connecting the inner and outer segments of photoreceptors, leading to photoreceptor degeneration, frequently the first feature of BBS to develop after birth [40,41]. BBS is the second most prevalent form of syndromic retinitis pigmentosa [42], after Usher syndrome. Unlike most forms of retinitis pigmentosa, BBS typically shows photoreceptor degeneration first in the macula.

We imaged a 5-month-old rhesus macaque with early-stage BBS with our device. The OCT volumetric data consisted of 768 A-lines per B-scan, 768 B-scan positions per volume, and 3 repeated scans per position. The animal's retina was imaged over a macular 6 × 6-mm region rather than the fully achievable field of view in order to improve sampling resolution since this disease is macula-involved. We were able to identify seven distinct retinal layers, the entire choroid and sclera, and the connective below the sclera (Fig. 3(A), B). The cross-sectional image was examined at the middle of the field of view and at a position 3 mm offset from the middle, both of which had a high signal-to-noise ratio and high penetration depth. Due to the BBS genetic disorder, there was a marked attenuation of the ellipsoid zone comprising the inner segment of the photoreceptors (Fig. 3(A), B). The number of tissue structures visible in this image (including deep regions that are more difficult to image in humans due to the relatively larger size of the eye) is another advantage of our system, since pathology in any of these locations could be assessed and correlated with pathology in others and granting a holistic picture of disease development in NHP eyes.

Subsequently, the volumetric data was segmented into different layers, and structural *en face* images were generated from the whole retina, the nerve fiber layer (NFL), deep capillary plexus (DCP; which includes the anatomic slab from the outer plexiform layer to the outer nuclear layer), and choroidal layer (Fig. 3(D), (E), (F)). The distribution of nerve fibers and capillaries could be observed, while in the deep layer, the distribution of capillaries could also be observed in the structural channel without OCTA processing. Imaged at this early stage of the BBS, no significant changes in retinal circulatory networks were apparent, and both retinal nerve fiber bundles and the choroidal capillary plexus had no significant degeneration.

OCTA images were also generated using the same data set. We were able to generate *en face* OCTA images of the superficial vascular plexus (SVC), intermedia capillary plexus (ICP), and deep capillary plexus (DCP) (Fig. 4(A)-(C)). The DCP image in (Fig. 4(C)) can be contrasted with the structural image of the same region in (Fig. 3(E)). The OCTA version more clearly highlights the vascular structure, but by comparison with the structure we can see that projection artifacts were successfully removed from the DCP image. It also lacks the large vessel shadows visible in the structural image. There is no obvious degeneration or disruption of capillaries in these images.

#### 3.3. Batten disease

Batten disease refers to a heterogenic group of neuronal ceroid lipofuscinoses [43]. These fatal conditions originate in mutations in genes encoding soluble lysosomal enzymes, integral

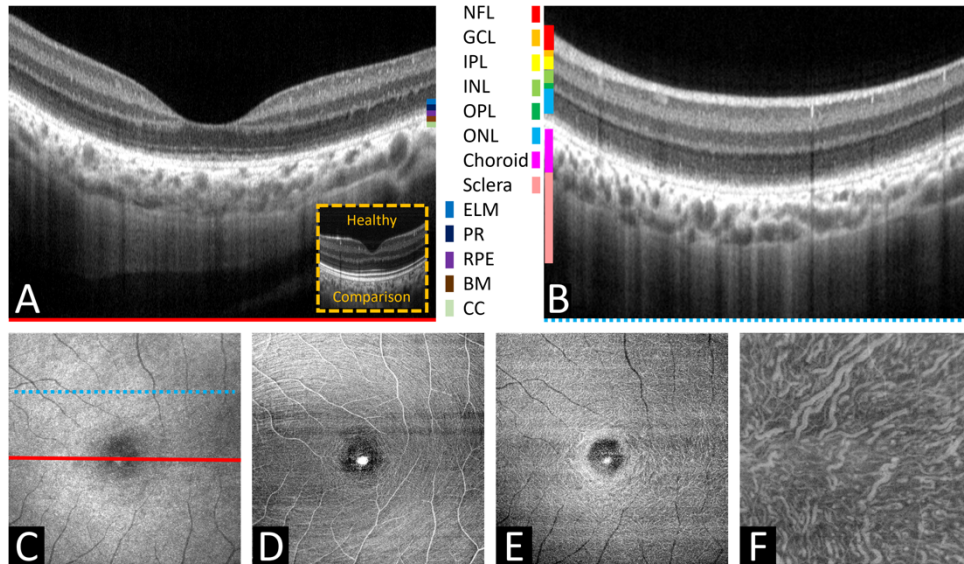


**Fig. 3.** Macular scan of an NHP with BBS. (A) High resolution OCT cross-sectional scan averaged across 5 B-frames of the central field of view, with healthy individual for comparison in inset. (B) High resolution OCT B-scan offset 2 mm from the center, averaging over the same number of B-scans. Thirteen different layers are color coded (on right, NFL: nerve fiber layer, GCL: ganglion cell layer, IPL: inner plexiform layer, INL: inner nuclear layer, OPL: outer plexiform layer, ONL: outer nuclear layer, the choroid, and sclera; on left, ELM: external limiting membrane, PR: photoreceptor layers, RPE: retinal pigment epithelium, BM: Bruch's membrane, CC: choriocapillaris are shown for clarity due to the thinness of these structures). In both (A) and (B), ellipsoid zone attenuation is apparent (compare inset from a healthy NHP in (A)). (C) *En face* projection across the whole imaging depth, with the location of the cross-sectional scans indicated by red (A) and blue (B) lines. (D) Nerve fiber layer structural image showing individual nerve fiber bundles (C). (E) Deep capillary plexus structural image with visible capillaries. (F) Choroidal structural projection.

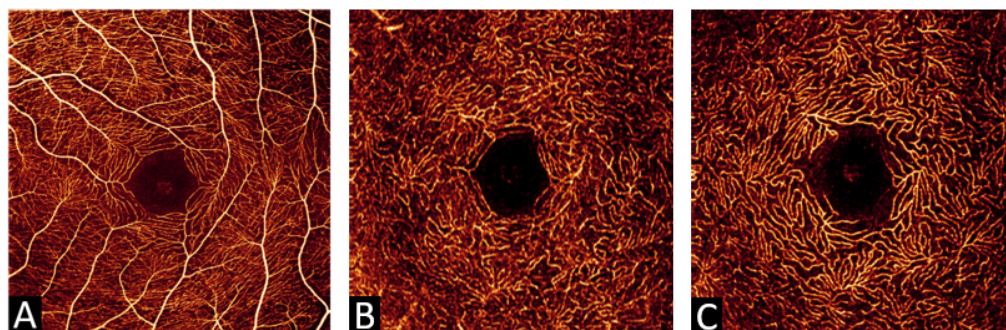


**Fig. 4.** OCTA from an NHP with BBS. (A) Superficial vascular plexus OCTA image, (B) intermediate capillary plexus image, and (C) deep capillary plexus OCTA image.

lysosomal trans-membrane proteins, endoplasmic reticulum membrane proteins, and cytosolic proteins that associate with vesicular membranes [44] that result in neuronal loss, especially in the cerebral cortex, cerebellum, and retina [45–47]. Similar to BBS, Batten disease often first presents as progressive loss of vision [43,48]. In OCT imaging, neuronal degeneration due to Batten disease can be identified by thinning the inner and outer retina [13].

Images from a subject with Batten disease and *CLN7* mutation were acquired. A 60° wide-field OCT image (Fig. 5(A)) was first acquired to evaluate gross retinal structural information. The volume contained 1024 A-lines per B-scan, 1024 B-scans per volume. Severe retinal thinning could be observed in the B-scan image (Fig. 5(B)). After applying the auto-generated segmentation result, the choroidal (Fig. 5(C)) capillary images could also be observed. OCTA images were also acquired in a high-density scan and smaller field of view in the 3 × 3-mm central macular region. Each volume contained 768 A-lines per B-scan, 768 B-scans per volume with 3 repeated scans at each position; we show the SVC (Fig. 5(D)) above. From the cross-section in particular (Fig. 5(E)) it can be seen that the normal plexus organization is lacking; i.e., distinct plexuses are not apparent (compare Fig. 2(D)). Instead, the vessels are mostly confined to a narrow depth. Choroidal flow is better imaged in the same central macular region using the structural channel (Fig. 5(F)), but can be acquired during the same procedure.

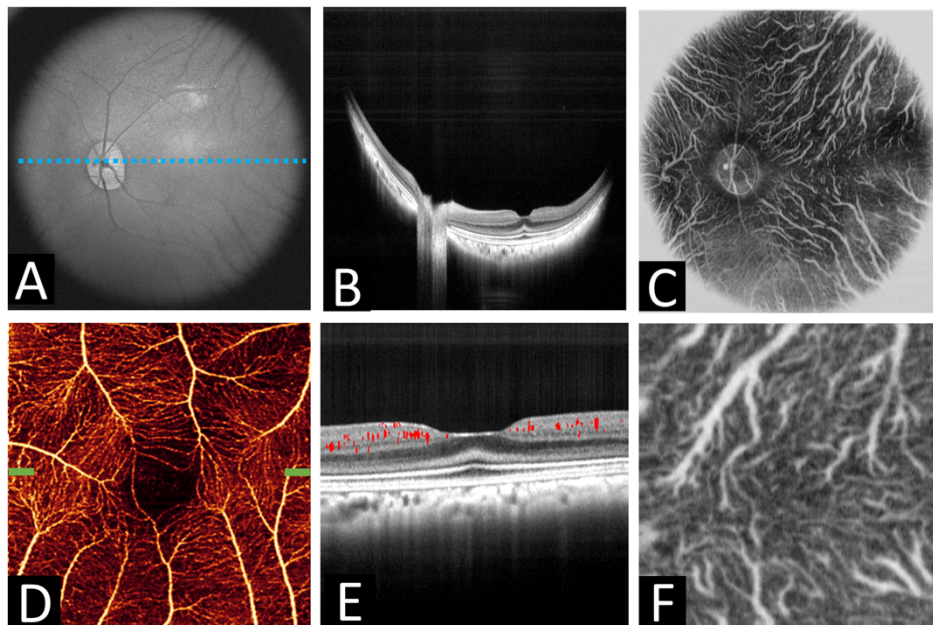


**Fig. 5.** Image acquired from a NHP with Batten disease and *CLN7* mutation. Top row: full 60-degree field-of-view scan. (A) *En face* OCT image projected across the retina. (B) OCT B-scan image across the center field of view (indicated by the dotted line in (A)), constructed by averaging over 5 B-scans. (C) *En face* projection from the choroid. Bottom row: a 3 × 3-mm scan of the same eye. (D) OCTA image of the inner retina. (E) Structural cross-section at the location of the green tick marks in (D) with retinal flow signal (red) overlaid, also constructed by averaging over 5 B-scans. Compared to a normal NHP the vessels in this animal do not form distinct plexuses. (F) 3 × 3-mm choroidal image in the structural channel.

### 3.4. Age-related macular degeneration

Age-related macular degeneration (AMD) is the most prevalent retinal degenerative disease [49] and a major area of research in ophthalmology [8,50]. Advanced states of the disease are characterized by either exudation or geographic atrophy, both of which can cause blindness [51]. While exudative AMD outcomes can be improved with anti-VEGF therapy [52,53], eyes undergoing this treatment can still develop geographic atrophy [54,55], which remains without therapeutic options with demonstrated benefits for vision [56,57]. Many older rhesus macaques show a drusenoid maculopathy that closely resembles the early to intermediate stages of AMD [10,58,59], and that can be accelerated by dietary manipulation [60].

A monkey with drusenoid maculopathy was imaged (Fig. 6). An OCT volume with 768 A-lines per B-scan and 768 B-scans per volume with 3 repeats was acquired in a 6 × 6-mm region centered at the macula. An *en face* OCT image was also generated (Fig. 6(A)), and abnormal hyper-reflectance was observed. In addition, RPE changes and drusen were observed from cross-sectional images in selected slices (Fig. 6(C)). OCTA images were also generated using the same data set. No significant capillary nonperfusion areas or other early-stage vascular pathologic changes can be observed in these images.

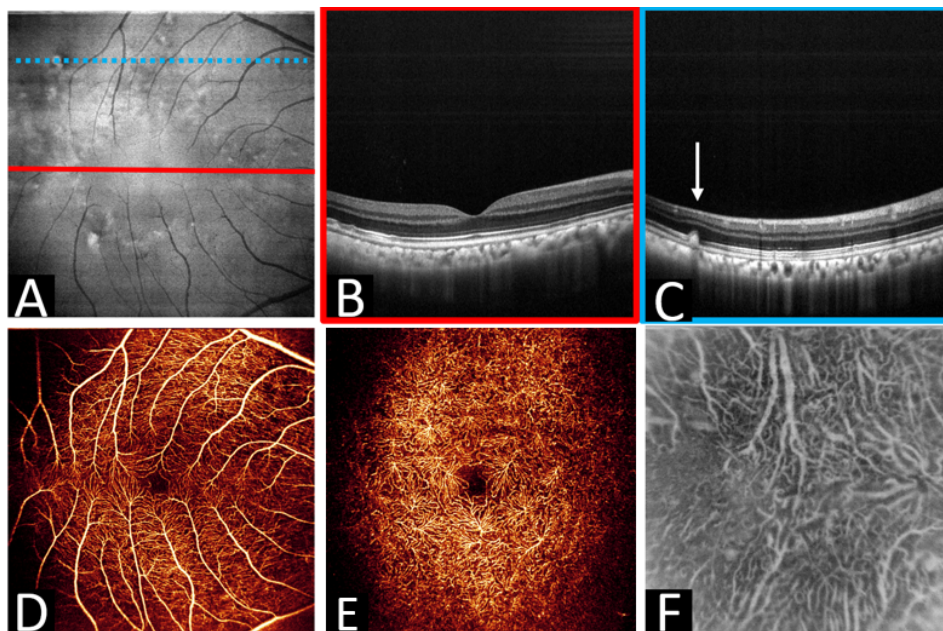


**Fig. 6.** 6 × 6-mm image acquired from a subject with AMD-like pathology. (A) Structural OCT images of the macula. (B) OCT cross-sectional image at the center field of view (location of the red line in (A)) showing abnormal hyper-reflectance. (C) OCT cross-sectional image in the superior region (the blue dotted line location in (A)), with drusen highlighted (white arrow). Both cross-sectional images were constructed by averaging over 5 B-scans. (D) OCTA *en face* image of the SVC. (E) OCTA image from DCP. (F) Structural choroidal image.

## 4. Discussion

In this report, we developed a swept-source OCTA device optimized for NHP imaging. Acquiring images from NHP models of three separate diseases, we demonstrated our device's capabilities for achieving high-resolution 60° field-of-view structural and angiographic images.

Recently, several research groups have used existing commercial OCT imaging devices for NHP studies, focusing mainly on quantifying retinal thickness [61]. But retinal thickness measurements are just one pathologic feature implicated in some retinal diseases. Other pathologic features such as the ellipsoid zone attenuation or peripheral drusen may have more stringent instrument design requirements in order to be clearly visualized. Wu et al. investigated the ability of a commercial device to achieve vascular imaging in NHPs, but their study was restricted to apparently healthy individuals and they noted the presence of projection artifacts in peripheral regions [62]. These artifacts are not apparent in our approach. While small eye settings on commercial OCT devices typically enable NHP imaging without hardware modification, this does not mean that these systems are optimized for such imaging.

Controlling aberrations across a large field of view is critical for achieving high-quality wide-field OCT/OCTA imaging. Optical imaging systems that are diffraction-limited have the ability to considerably enhance image quality, image contrast, and the signal-to-noise ratio. The design of the sample arm optics plays an important role in OCT system development. Unlike other lens-based imaging systems that use customized lenses and imaging sensors to acquire images, ocular imaging systems adopt both customized lenses and the optics of the eye to achieve high-resolution images of the retina. The imperfections of the eye's optics and the optical system contribute to most aberrations. Specifically, when scanning at large angles, aberrations can make it difficult to obtain clear peripheral OCT images in wide-field OCT/OCTA imaging. Designing the sample arm optics with care can alleviate this problem and significantly reduce system aberrations.

In this study, we used computational methods in lens design and optical system evaluation to determine a customized lens set for a non-human primate ocular imaging device. We used a model eye to characterize the scanning and ocular lens's performance and achieved a diffraction-limited performance based on simulation results. The largely artifact-free images we obtained resulted from these simulations (Fig. 4), enabling detailed pathology assessment in the NHP models imaged in this study. This design achieved both a large transverse field-of-view and could image from the vitreous down to the connective tissue of the sclera.

Another advantage of our approach is efficient OCTA signal generation. Real-time OCTA is essential for acquiring OCTA images with a large field of view, which is critical for monitoring optimal imaging position and angle. In recent years, the development of high-performance graphics processing unit (GPU) technology and highly efficient GPU algorithms has enabled real-time OCTA image acquisition on personal computers. However, the efficiency and performance of OCTA algorithms still play a critical role in achieving optimal OCTA imaging results. Developing high-efficiency and high-performance OCTA algorithms is necessary to reduce image acquisition time, improve image quality, and accurately quantify blood flow in ocular tissues. In this study, we adapted our previous GPU-based real-time OCT/OCTA techniques [32] for human eye imaging to a non-human primate imaging system in order to improve data acquisition efficiency and the yield rate of high-quality images.

This study has limitations. Some performance issues still need to be addressed in our system. The imperfection of NHP eye optics contributes to most aberrations, making it challenging to achieve diffraction-limited imaging without an adaptive solution. Many groups have developed ocular imaging systems that adopt adaptive optics techniques to achieve diffraction-limited imaging on the retina. Another challenge is imaging sedated animals, where aligning the eye's optical axis and the imaging system's optical axis is critical for high-quality scan acquisition. Due to the lack of freedom in our current optical mount, the alignment is often imperfect, highlighting the need for improved optomechanical design. Finally, the number of NHPs imaged in this study was small and included individuals exhibiting mostly early-stage pathologic features for the diseases assessed. Future work will examine more NHPs to quantify and visualize more varied pathologic features than we were able to catalog in this report.

## 5. Conclusion

In this study, we presented a high-performance OCT/OCTA imaging system that can acquire high-quality images with ultra-fine details of retinal structure and vasculature across a 60° field-of-view from the vitreous to sclera and connecting tissue. Our optical system design played a critical role in achieving these results by minimizing aberrations and improving the imaging resolution. The real-time OCT/OCTA software also significantly improved the data acquisition efficiency, enabling us to obtain a large volume of high-quality images in a short period. We imaged multiple NHP disease models, including BBS, Batten disease with *CLN7* mutation, and drusenoid maculopathy to demonstrate the significance of this utility modality. The high-resolution images obtained using our system clearly visualized pathologic features which could be valuable tools for early detection and monitoring disease progression, including drusen, retinal thinning, and loss of plexus organization. Our results highlight the potential of OCT/OCTA imaging as a non-invasive, high-resolution imaging modality for NHP ocular disease studies.

**Funding.** BrightFocus Foundation (G2020168, M20230081); Noah's Hope; Batten Disease Support and Research Association; Edward N. and Della L. Thome Memorial Foundation; Research to Prevent Blindness Stein Innovation Award; Dr. H. James and Carole Free Catalyst Award; Unrestricted Departmental Funding Grant; Malcolm M. Marquis, MD Endowed Fund for Innovation; National Institutes of Health (NIH) (P30 EY010572, P51 OD011092, R01 EY023285, R01 EY024544, R01 EY027833, R01 EY028141, R01 EY031394, R01 EY035309, R01 EY035410, R01 EY036429, R24 NS104161, T32 EY023211, UL1TR002369).

**Acknowledgments.** This work was supported by the National Institute of Health (R01 EY035410, R01 EY027833, R01 EY024544, R01 EY031394, R01EY036429, R01 EY023285, R01 EY035309, R01 EY028141, R24 NS104161, T32 EY023211, UL1TR002369, P30 EY010572, P51 OD011092); the Malcolm M. Marquis, MD Endowed Fund for Innovation; an Unrestricted Departmental Funding Grant, Dr. H. James and Carole Free Catalyst Award, Stein Innovation Award from Research to Prevent Blindness (New York, NY), Edward N. & Della L. Thome Memorial Foundation Award, Batten Disease Research and Support Association, Noah's Hope, and the Bright Focus Foundation (G2020168, M20230081).

**Disclosures.** Oregon Health & Science University (OHSU) and Dr. Yali Jia have a significant financial interest in Optovue/Visionix, Inc. Genentech Inc. and Optos, Inc. These potential conflicts of interest have been reviewed and managed by OHSU.

**Data Availability.** Data underlying the results presented in this paper are not publicly available at this time but may be obtained from the authors upon reasonable request.

## References

1. D. Huang, E. A. Swanson, C. P. Lin, *et al.*, "Optical coherence tomography," *Science* **254**(5035), 1178–1181 (1991).
2. B. Lumbroso, D. Huang, C. J. Chen, *et al.*, "Waheed, *Clinical OCT Angiography Atlas* (JP Medical Ltd, 2015).
3. M. G. Ducros, J. D. Marsack, H. G. Rylander, *et al.*, "Primate retina imaging with polarization-sensitive optical coherence tomography," *J. Opt. Soc. Am. A* **18**(12), 2945 (2001).
4. X. Wei, T. T. Hormel, S. Pi, *et al.*, "Wide-field sensorless adaptive optics swept-source optical coherence tomographic angiography in rodents," *Opt. Lett.* **47**(19), 5060 (2022).
5. G. Huber, S. C. Beck, C. Grimm, *et al.*, "Spectral domain optical coherence tomography in mouse models of retinal degeneration," *Invest. Ophthalmol. Vis. Sci.* **50**(12), 5888–5895 (2009).
6. S. Hariri, M. C. Tam, D. Lee, *et al.*, "Noninvasive imaging of the early effect of sodium iodate toxicity in a rat model of outer retina degeneration with spectral domain optical coherence tomography," *J. Biomed. Opt.* **18**(2), 026017 (2013).
7. J. L. Edelman, D. Lutz, and M. R. Castro, "Corticosteroids inhibit VEGF-induced vascular leakage in a rabbit model of blood-retinal and blood-aqueous barrier breakdown," *Exp. Eye Res.* **80**(2), 249–258 (2005).
8. L. S. Lim, P. Mitchell, J. M. Seddon, *et al.*, "Age-related macular degeneration," *Lancet* **379**(9827), 1728–1738 (2012).
9. Diabetic Retinopathy Clinical Research Network, "Relationship between OCT-measured central retinal thickness and visual acuity in diabetic macular edema," *Ophthalmology* **114**, 525–536 (2008).
10. P. J. Francis, B. Appukuttan, E. Simmons, *et al.*, "Rhesus monkeys and humans share common susceptibility genes for age-related macular disease," *Hum. Mol. Genet.* **17**(17), 2673–2680 (2008).
11. P. Gouras, L. Ivert, N. Landauer, *et al.*, "Drusenoid maculopathy in rhesus monkeys (*Macaca mulatta*): Effects of age and gender," *Graefes Arch. Clin. Exp. Ophthalmol.* **246**(10), 1395–1402 (2008).
12. S. M. Peterson, T. J. McGill, T. Puthussery, *et al.*, "Bardet-Biedl Syndrome in rhesus macaques: A nonhuman primate model of retinitis pigmentosa," *Exp. Eye Res.* **189**, 107825 (2019).

13. J. L. McBride, M. Neuringer, B. Ferguson, *et al.*, "Discovery of a CLN7 model of Batten disease in non-human primates," *Neurobiol. Dis.* **119**, 65–78 (2018).
14. R. Leitgeb, C. K. Hitzenberger, and A. F. Fercher, "Performance of fourier domain vs time domain optical coherence tomography," *Opt. Express* **11**(8), 889–894 (2003).
15. M. Wojtkowski, R. Leitgeb, A. Kowalczyk, *et al.*, "In vivo human retinal imaging by Fourier domain optical coherence tomography," *J. Biomed. Opt.* **7**(3), 457 (2002).
16. M. A. Choma, M. V. Sarunic, C. Yang, *et al.*, "Sensitivity advantage of swept source and Fourier domain optical coherence tomography," *Opt. Express* **11**(18), 2183–2189 (2003).
17. T. Klein, W. Wieser, C. M. Eigenwillig, *et al.*, "Megahertz OCT for ultrawide-field retinal imaging with a 1050 nm Fourier domain mode-locked laser," *Opt. Express* **19**(4), 3044 (2011).
18. J. P. Kolb, T. Klein, C. L. Kufner, *et al.*, "Ultra-widefield retinal MHz-OCT imaging with up to 100 degrees viewing angle," *Biomed. Opt. Express* **6**(5), 1534–1552 (2015).
19. M. Niederleithner, L. De Sisternes, H. Stino, *et al.*, "Ultra-Widefield OCT Angiography," *IEEE Trans. Med. Imaging* **42**(4), 1009–1020 (2023).
20. J. P. Su, R. Chandwani, S. S. Gao, *et al.*, "Calibration of optical coherence tomography angiography with a microfluidic chip," *J. Biomed. Opt.* **21**(08), 1 (2016).
21. Z. Wang, B. Potsaid, L. Chen, *et al.*, "Cubic meter volume optical coherence tomography," *Optica* **3**(12), 1496 (2016).
22. S. Song, J. Xu, and R. K. Wang, "Long-range and wide field of view optical coherence tomography for in vivo 3D imaging of large volume object based on akinetic programmable swept source," *Biomed. Opt. Express* **7**(11), 4734 (2016).
23. B. Liu and M. E. Brezinski, "Theoretical and practical considerations on detection performance of time domain, Fourier domain, and swept source optical coherence tomography," *J. Biomed. Opt.* **12**(4), 044007 (2007).
24. Z. Chen, M. Liu, M. Minneman, *et al.*, "Phase-stable swept source OCT angiography in human skin using an akinetic source," *Biomed. Opt. Express* **7**(8), 3032 (2016).
25. S. Moon and Z. Chen, "Phase-stability optimization of swept-source optical coherence tomography," *Biomed. Opt. Express* **9**(11), 5280 (2018).
26. X. Wei, T. T. Hormel, and Y. Jia, "Phase-stabilized complex-decorrelation angiography," *Biomed. Opt. Express* **12**(4), 2419–2431 (2021).
27. N. Huang, T. Hormel, G. Liang, *et al.*, "Optimizing numerical k-sampling for swept-source optical coherence tomography angiography," *Opt. Lett.* **49**(5), 1201–1204 (2024).
28. T. T. Hormel, Y. Jia, Y. Jian, *et al.*, "Plexus-specific retinal vascular anatomy and pathologies as seen by projection-resolved optical coherence tomographic angiography," *Prog. Retinal Eye Res.* **80**, 100878 (2021).
29. *American National Standard for Safe Use of Lasers (ANSI Z136.1-2014)* (2014).
30. X. Wei, T. T. Hormel, Y. Guo, *et al.*, "75-degree non-mydriatic single-volume optical coherence tomographic angiography," *Biomed. Opt. Express* **10**(12), 6286–6295 (2019).
31. T. T. Hormel, G. B. Liang, X. Wei, *et al.*, "Visualizing features with wide-field volumetric OCT angiography," *Opt. Express* **32**(6), 10329 (2024).
32. X. Wei, A. Camino, S. Pi, *et al.*, "Real-time cross-sectional and en face OCT angiography guiding high-quality scan acquisition," *Opt. Lett.* **44**(6), 1431 (2019).
33. A. Fercher, C. Hitzenberger, M. Sticker, *et al.*, "Numerical dispersion compensation for Partial Coherence Interferometry and Optical Coherence Tomography," *Opt. Express* **9**(12), 610 (2001).
34. Y. Guo, A. Camino, M. Zhang, *et al.*, "Automated segmentation of retinal layer boundaries and capillary plexuses in wide-field optical coherence tomographic angiography," *Biomed. Opt. Express* **9**(9), 4429–4442 (2018).
35. M. Zhang, J. Wang, A. D. Pechauer, *et al.*, "Advanced image processing for optical coherence tomographic angiography of macular diseases," *Biomed. Opt. Express* **6**(12), 4661 (2015).
36. T. T. Hormel, J. Wang, S. T. Bailey, *et al.*, "Maximum value projection produces better en face OCT angiograms than mean value projection," *Biomed. Opt. Express* **9**(12), 6412–6424 (2018).
37. G. Bardet, "On congenital obesity syndrome with polydactyly and retinitis pigmentosa," *Obes. Res.* **3**(4), 387–399 (1995).
38. A. Biedl, "A pair of siblings with adiposo-genital dystrophy," *Obes. Res.* **3**(4), 404 (1995).
39. P. L. Beales, N. Elcioglu, A. S. Woolf, *et al.*, "New criteria for improved diagnosis of Bardet-Biedl syndrome: results of a population survey," *J. Med. Genet.* **36**(6), 437–446 (1999).
40. A. Mockel, Y. Perdomo, F. Stutzmann, *et al.*, "Retinal dystrophy in Bardet-Biedl syndrome and related syndromic ciliopathies," *Prog. Retinal Eye Res.* **30**(4), 258–274 (2011).
41. K. M. Bujakowska, Q. Liu, and E. A. Pearce, "Photoreceptor cilia and retinal ciliopathies," *Cold Spring Harbor Perspect. Biol.* **9**(10), a028274 (2017).
42. E. Forsythe and P. L. Beales, "Bardet-Biedl syndrome," *Eur. J. Hum. Genet.* **21**(1), 8–13 (2013).
43. M. Kousi, A. E. Lehesjoki, and S. E. Mole, "Update of the mutation spectrum and clinical correlations of over 360 mutations in eight genes that underlie the neuronal ceroid lipofuscinoses," *Hum. Mutat.* **33**(1), 42–63 (2012).
44. J. Cárcel-Trullols, A. D. Kovács, and D. A. Pearce, "Cell biology of the NCL proteins: What they do and don't do," *Biochim. Biophys. Acta, Mol. Basis Dis.* **1852**(10), 2242–2255 (2015).
45. G. W. Anderson, H. H. Goebel, and A. Simonati, "Human pathology in NCL," *Biochim. Biophys. Acta, Mol. Basis Dis.* **1832**(11), 1807–1826 (2013).

46. J. D. Cooper, M. A. Tarczyluk, and H. R. Nelvagal, "Towards a new understanding of NCL pathogenesis," *Biochim. Biophys. Acta, Mol. Basis Dis.* **1852**(10), 2256–2261 (2015).
47. D. N. Palmer, L. A. Barry, J. Tyynelä, *et al.*, "NCL disease mechanisms," *Biochim. Biophys. Acta, Mol. Basis Dis.* **1832**(11), 1882–1893 (2013).
48. R. E. Williams and S. E. Mole, "New nomenclature and classification scheme for the neuronal ceroid lipofuscinoses," *Neurology* **79**(2), 183–191 (2012).
49. W. L. Wong, X. Su, X. Li, *et al.*, "Global prevalence of age-related macular degeneration and disease burden projection for 2020 and 2040: A systematic review and meta-analysis," *Lancet Global Health* **2**(2), e106–e116 (2014).
50. R. Flores, A. Carneiro, M. Vieira, *et al.*, "Age-related macular degeneration: pathophysiology, management, and future perspectives," *Ophthalmologica* **244**(6), 495–511 (2021).
51. F. L. Ferris, C. P. Wilkinson, A. Bird, *et al.*, "Clinical classification of age-related macular degeneration," *Ophthalmology* **120**(4), 844–851 (2013).
52. J. S. Heier, D. M. Brown, V. Chong, *et al.*, "Intravitreal afibercept (VEGF trap-eye) in wet age-related macular degeneration," *Ophthalmology* **119**(12), 2537–2548 (2012).
53. D. M. Brown, P. K. Kaiser, M. Michels, *et al.*, "Ranibizumab versus verteporfin for neovascular age-related macular degeneration," *N. Engl. J. Med.* **355**(14), 1432–1444 (2006).
54. J. E. Grunwald, M. Pistilli, E. Daniel, *et al.*, "Incidence and growth of geographic atrophy during 5 years of comparison of age-related macular degeneration treatments trials," *Ophthalmology* **124**(1), 97–104 (2017).
55. S. Rofagha, R. B. Bhisitkul, D. S. Boyer, *et al.*, "Seven-year outcomes in ranibizumab-treated patients in ANCHOR, MARINA, and HORIZON: A multicenter cohort study (SEVEN-UP)," *Ophthalmology* **120**(11), 2292–2299 (2013).
56. R. Goldberg, J. S. Heier, C. C. Wykoff, *et al.*, "Efficacy of intravitreal pegcetacoplan in patients with geographic atrophy (GA): 12-month results from the phase 3 OAKS and DERBY studies," *Invest. Ophthalmol. Vis. Sci.* **63**, 1500 (2022).
57. D. S. Liao, F. V. Grossi, D. El Mehdi, *et al.*, "Complement C3 inhibitor pegcetacoplan for geographic atrophy secondary to age-related macular degeneration: a randomized Phase 2 Trial," *Ophthalmology* **127**(2), 186–195 (2020).
58. M. E. Pennesi, M. Neuringer, and R. J. Courtney, "Animal models of age-related macular degeneration," *Mol. Aspects Med.* **33**(4), 487–509 (2012).
59. P. Gouras, L. Ivert, J. A. Mattison, *et al.*, "Drusenoid maculopathy in rhesus monkeys: Autofluorescence, lipofuscin and drusen pathogenesis," *Graefe's Arch. Clin. Exp. Ophthalmol.* **246**(10), 1403–1411 (2008).
60. T. J. McGill, L. M. Renner, and M. Neuringer, "Elevated fundus autofluorescence in monkeys deficient in lutein, zeaxanthin, and omega-3 fatty acids," *Invest. Ophthalmol. Vis. Sci.* **57**(3), 1361–1369 (2016).
61. V. V. Srinivasan, S. Das, and N. Patel, "Widefield OCT imaging for quantifying inner retinal thickness in the nonhuman primate," *Trans. Vis. Sci. Tech.* **11**(8), 12 (2022).
62. X. Wu, J. Chua, C. Ho, *et al.*, "In-vivo imaging of ocular microvasculature using swept-source optical coherence tomography angiography in seven types of lab animals," *Front. Photon.* **3**, 12 (2022).